State diagram of nanopillar spin valves with perpendicular magnetic anisotropy

S. Le Gall, J. Cucchiara, M. Gottwald, C. Berthelot, C.-H. Lambert, Y. Henry, D. Bedau, D. B. Gopman, H. Liu, A. D. Kent, J. Z. Sun, W. Lin, D. Ravelosona, J. A. Katine, Eric E. Fullerton, and S. Mangin

Phys. Rev. B **86**, 014419 — Published 18 July 2012

DOI: 10.1103/PhysRevB.86.014419

State diagram of nanopillar spin-valve with perpendicular magnetic anisotropy

S. Le Gall[1], J. Cucchiara[1], M. Gottwald[1], C. Berthelot[1], C-H. Lambert[1]
[1]*Institut Jean Lamour, CNRS – Nancy Université, Vandoeuvre lès Nancy, France*

Y. Henry[2]
[2]*Institut de Physique et Chimie des Matériaux de Strasbourg, CNRS – UDS, France*

D. Bedau[3], D. B. Gopman[3], H. Liu[3], A. D. Kent[3]
[3]*Department of Physics, New York University, New York 10003, USA*

J. Z. Sun[4]
[4]*IBM T. J. Watson Research Center, Yorktown Heights, New York 10598, USA*

W. Lin[5], D. Ravelosona[5]
[5]*Institut d'Electronique Fondamentale, UMR CNRS 8622, Université Paris Sud, France*

J. A. Katine[6]
[6]*Hitachi Global Storage Technologies, San Jose Research Center, CA, USA*

Eric E. Fullerton[7]
[7]*Center of Magnetic Recording Research, University of California San Diego, CA, USA*

S. Mangin[1]
[1]*Institut Jean Lamour, CNRS – Nancy Université, Vandoeuvre lès Nancy, France*

Abstract

The spin-torque switching of metallic nanopillar spin-valves showing strong perpendicular anisotropy are studied. The magnetic states of the layers depend on extrinsic parameters such as the magnetic field and the DC current applied to the device. A state diagram presents a comprehensive graph the role of those parameters on the spin-valve magnetic response. After explaining how state diagrams can be built and the different possible representation, experimental state diagram are studied for perpendicular devices and the influence of lateral size, temperature and field orientation are shown. An analytical model of a purely uniaxial system is presented. It is shown that this simple model does not properly reflect the experimental results whereas if the symmetry is broken a qualitative agreement is obtained. Finally the possible origins of the symmetry break are discussed in the light of analytical model and numerical simulations.

I. Introduction

The possibility to manipulate and control the magnetization of a magnetic nano-object using a spin-polarized current was predicted by both Luc Berger [1-3] and John Slonczewski [4]. As a consequence of angular moment conservation, a spin-polarized current may transfer angular momentum to a nanomagnetic that acts as a torque acting on the magnetization. This spin transfer torque will add to the field and damping torques to provide the Landau-Lifshitz-Gilbert-Slonczewski (LLGS) equation which describes magnetization dynamics in the presence of an effective field and an injected current [5]. Not only does this new torque affect the magnetization dynamics, it also induces new magnetization states that cannot be stabilized using external static or dynamic magnetic fields [6]. These new magnetization states are either static states that are not an energy minima or steady precessional states. Consequently several new phenomena could be observed such as magnetization steady state precessions, vortex precession and current-induced magnetization switching as recently reviewed in Refs. [7-9].

Experimentally it was first demonstrated that spin polarized electrons could propagate a domain wall in a wire [10]. Since then, domain propagation assisted by a polarized current has been studied extensively involving different domain wall type, different materials, different geometries [11-13]. The understanding of the fundamental physics ruling domain wall propagation allows the possibility of applications in the field of magnetic data storage as the "Race track memories" proposed by Stuart Parkin [14].

Experimental measurements of current-induced resistance changes were first done in magnetic multilayers with spin torque driven excitations in 1998 [15] and then in magnetic oxide junctions in 1999 [16]. In 2000, magnetization reversal of a magnetic nano-object under a polarized current using a nanopillar spin-valve was demonstrated [17]. This has spurred extensive research in metallic spin-valve and magnetic tunnel junction (MTJ) nanopillar structures and development of new applications including spin-transfer torque magnetic random access memories (STT-MRAMs) and rf devices such as current-tunable microwave nano-oscillators (STNO) [18-21]. Implementation of STT-MRAM requires low critical currents to switch the nanomagnet while maintaining sufficient thermal stability [21]. Toward this goal nanopillars with perpendicular magnetic anisotropy (PMA) have shown to be particularly interesting since they provide a way to lower the switching current. Indeed, as shown and described in this paper the perpendicular geometry has a number of advantages over in-plane devices. The magnetic response is more strongly determined by the intrinsic properties of the materials rather than being dominated by the shape of the device. PMA is controllable by judicious engineering of material properties. High anisotropy materials with strong PMA provide stability against thermal activation down to smaller nanomagnet sizes than feasible with shape anisotropy alone [22]. Moreover, PMA materials provide a model system to investigate the combine effect of applied magnetic field (H) and injected current (I). We shall then concentrate on the study of a state diagram (also called phase diagram, switching diagram or stability diagram in the literature) which is a map of the equilibrium magnetic states available in the (H, I) parameter space similar to what was described earlier in Ref. 23. The state diagram gives a complete and readable picture on the impact of the applied magnetic field and of the spin polarized current on the magnetization. In the literature, both experimental and theoretical state diagrams in (H, I) or (H, V) space were done previously for spin valves with in plane [18, 23-49], perpendicular [50-58] or both [59-61] anisotropy, and for MTJs [62-78]. The aim of the paper is then to describe in detail how to measure, model and interpret such a state diagram with the goal to understand the effect of the intrinsic (linked

to the materials properties) and the extrinsic parameters (controlled during the experiments) on the magnetization state.

We will focus on spin-valve structures with PMA for which their magnetic layers have an easy anisotropy axis pointing in the out-of-plane direction. Spin-valves with both the polarizer and the free layer having PMA is a uniaxial model system. Indeed all the contributions (fields, anisotropy axis, and current) in this system are expected to be aligned along the same perpendicular axis. Perpendicular geometry also provides a way to decrease the switching current required to observe current-induced magnetization reversal [50, 79-82]. The reason of the larger magnetization reversal efficiency for the perpendicular case compared to the in-plane one comes from the effect of the demagnetizing field in the two geometries. Figure 1 and Table I point out the differences between these two cases. In the analytical expression of the switching current required to reverse the magnetization in the in-plane case, a constant term due to the demagnetization field is in addition to the in-plane anisotropy that suppresses reversal. In the perpendicular case the switching current is directly proportional to the height of the energy barrier between the parallel and the antiparallel states (U_K). For applications $U_K > 50\ k_BT$ is required to ensure 10 years stability. By controlling U_K and optimizing materials properties such as spin polarization and magnetic damping, the critical switching current can be reduced by more than one order of magnitude, while maintaining thermal stability [51, 83]. Note that in perpendicular anisotropy structures with composite free layers it should be possible to further decrease the critical switching current while maintaining stability [84].

In this paper we focus on nanopillar spin-valves with PMA, under the application of a magnetic field and an injected current by studying the state diagrams. In section II, after a brief description of the spin valves studied here, we explain how to measure, to plot and interpret such a state diagram. Section III focuses on the analytical modeling based on a macrospin approach with uniaxial anisotropy symmetry to determine the theoretical state diagram of our samples. The comparison with the experimental results is presented on Section IV. We focus on the influences of extrinsic and intrinsic parameters as lateral size of the sample, temperature, sweeping field rate, time measurement and field orientation. We then conclude that to explain our experimental results, the symmetry of the system must be broken. Consequently, in section V, we refine our modeling by considering a non-uniaxial symmetry. Finally, in section VI, some possible origins of the symmetry breaking as a misalignment of the magnetic field or the anisotropy field as well as the presence of a higher order anisotropy constant are tested using numerical simulations.

II. Experimental state diagrams

The nanopillar spin-valve structures discussed in this paper have been reported in several papers before [50-55]. They are made of Co/Pt and Co/Ni multilayers with PMA that were grown both by co-evaporation and dc magnetron sputtering. The magnetic structure consists of a Pt(3 nm)/$[$Co(0.25 nm)/Pt(0.52 nm)$]_{x5}$/Co(0.2 nm)/$[$Ni(0.6 nm)/Co(0.1 nm)$]_{x2}$/Co(0.1 nm) hard reference layer and a Co(0.1 nm)/$[$Co(0.1 nm)/Ni(0.6 nm)$]_{x4}$/Pt(3 nm) free layer separated by a 4 nm Cu spacer layer. The multilayers were then patterned using electron beam lithography and ion etching into nanopillars of different shape (circle, hexagon…) of size varying from 50nm to 5µm. Two types of resistance are measured DC Resistance (R_{dc}=V/I) and AC resistance (R_{ac}=dV/dI). R_{dc} is measured by injecting a dc current (I_{dc}) and measuring voltage with a nano-voltmeter in a four terminal configuration. In that case I_{dc} is used both to

measure R_{dc} and to inject the current needed for spin transfer torque. The resistance dV/dI i.e the dV response to a small ac current oscillation dI measures R_{ac} [85] (see for instance Fig. 2 and 4). This is done using a lock-in technique. The two resistances are related as followed

$$R_{ac} = \frac{dV}{dI} = \frac{d(RI)}{dI} = R_{dc} + I\frac{dR}{dI} \quad (1)$$

As a consequence they are complementary since as soon as the resistance will be affected by the current reversibly as in the case of Joule heating or spin transfer torque effects the two resistances will differ. For instance, in the case of the onset of magnetization precession the resistance changes reversibly with current giving rise to a smooth R_{dc} variation but a peak in R_{ac}. The current is defined positive when the electrons flow from the reference layer to the free layer tending to align the two layers in the parallel state (P). The reference layer magnetization switches for an applied field close to 1 T. Since no fields greater than 0.5 T are applied during the measurements the reference layer is expected to be stable. For all the experiments shown here the reference layer magnetization is pinned along the positive field direction. As presented in previous studies [52] the dipolar stray field H_{dip} arising from the reference layer is acting on the free layer and affects the magnetization dynamic.

The experimental state diagrams are built by taking a series of field hysteresis loops for different injected currents (or are a series of current loops at different applied magnetic field). An example curve is shown in Fig. 2 showing hysteretic switching of the free layer. Indeed, for one value of the injected current a field hysteresis loop divides the magnetic field axis into three regions of different magnetic configurations. In the middle, it is the bistable region where spin-valve can be either in the parallel or antiparallel states. Going to the positive field, only the parallel configuration becomes available whereas going to the negative field, only the antiparallel configuration becomes available. The two borders between these three regions are marked by the switching fields (see Fig. 2(a)). Therefore, a plot of the evolution of these switching fields as a function of the injected current gives a state diagram.

To build a state diagram, we make a two-dimensional plot of either $R_{diff}(H) = R_{inc}(H) - R_{dec}(H)$ or $R_{sum}(H) = \frac{1}{2}[R_{inc}(H) + R_{dec}(H)]$ for different current values (see Figs. 2(b) and 2(c)) where $R_{inc}(H)$ and $R_{dec}(H)$ are the field increasing and decreasing branch of the hysteresis loop respectively (see Fig. 2(a)). With these two methods, the state diagram is then obtained by building a two dimensional colored map in the (H, I) parameter space where each point corresponds to a specific couple of current and field. Its color is given by the value of R_{diff} or R_{sum} at these coordinates (see Fig. 3). Each of its lines corresponds to a unique value of the injected current and is determined from the field hysteresis loop measured at this current. The qualitative difference between R_{sum} and R_{diff} is that R_{diff} highlight the hysteretic regions of the state diagram, as non-hysteretic regions will be zero.

In order to compare the lines obtained for different injected currents, the parabolic evolution of the nanopillar resistance due to the Joule heating has to be taken into account. Using the treatment with R_{diff} this problem disappears because the giant magnetoresistance ratio is not affected by the Joule heating. On the contrary, using R_{sum}, this effect induces a vertical contrast that can complicate the reading of the state diagram. To remove this contribution, the resistance values of the concerned hysteresis curves need to be normalize using the following formula $R_{norm} = (R-R_P)/(R_{AP}-R_P)$. As a result, the normalized resistances of the parallel and of the antiparallel states are respectively 0 and 1 (see Fig. 2(c)). Figure 3 presents the state diagram of a nanopillar spin-valve with perpendicular magnetizations similar to the previous

ones where Fig. 3(a) is R_{diff} and Fig. 3(b) R_{sum}. These two state diagrams exhibit a similar behavior. However, R_{diff} highlights the bistable region whereas R_{sum} highlights the behavior of the nanopillar in the high field and current regions. These two treatments are therefore complementary.

Figure 4 shows the same state diagram as Fig. 3(b) along with three characteristic hysteresis loops for three different injected currents values. These field hysteresis loops are horizontal cross-sections of the state diagram at the ordinate given by the value of the injected current. Similarly, a current hysteresis loop is a vertical cross-section of the state diagram at the abscissa given by the value of the applied magnetic field. The state diagram gathers the information given by field and current hysteresis loops. As mentioned previously, a state diagram is mainly divided into three regions: one for which the spin-valve is in the parallel state, one where it is in the antiparallel state and one where it can be in these two states, the bistable region. Because of our experimental conventions, the parallel state region is for the positive field and current (the blue region in Fig. 4) whereas the antiparallel state region is for the negative field and current region (the red region in Fig. 4). Between these two regions we find the bistable region (the green region in Fig. 4). A field hysteresis loop crossing these three regions gives a curve such as the one represented for I = 0 mA. The switching fields are given by the left and right limits of the bistable region whereas the switching currents are given by the up and down limits of the bistable region. Furthermore, two additional regions appear if the current and the field are large enough. Going to the positive currents the width of the hysteresis loop shrinks because of the spin transfer efficiency difference between the parallel to antiparallel and the antiparallel to parallel transitions. Consequently, in the upper left corner corresponding to a high positive current and a high negative field, the hysteresis loop ends up disappearing. Instead of a hysteretic behavior, the spin-valve transitions reversibly between the parallel and the antiparallel state passing through similar magnetic states. This region is generally characterized by peaks in R_{ac} [53] as seen in the R_{ac} vs H curve at I = 11 mA in Fig. 4. The width of these peaks appears in orange in the state diagram and they are shown to be the consequence of magnetization precessions [55]. These peaks should not appear in the state diagram obtained from the difference of resistances method because the increasing and the decreasing part of the hysteresis curve are reversible and, in principal, identical. Actually, their position between the increasing and the decreasing parts of the hysteresis are slightly shifted because of the field sweep procedure, so the difference of resistance gives a positive value at one side of the peak and a negative one on the other side. Consequently, the peaks appear as a couple of blue and red lines (see Fig. 3(a)) more complicated to interpret than in the representation with the R_{sum} treatment.

In the opposite corner corresponding to a high negative current and a high positive field the hysteresis loop also shrinks and even, at times, disappears. Here, the AC resistance curves are often characterized by a mix of small hysteretic regions, peaks and shoulders like in the curve measured at I = -13 mA. The hysteretic part and the peak appear as a pink coloration inside the bistable region.

Now that we have described the general shape of the experimental state diagrams of a nanopillar spin-valve with PMA, we will compare these results to modeled results.

III. Theoretical state diagram for a macrospin in uniaxial anisotropy

Throughout this study, we will consider a macrospin approximation at zero-temperature. We focus on a simple uniaxial anisotropy symmetry approach to describe the system. For this symmetry, the contributions of the effective magnetic field, the magnetization, the polarizer layer and current are along the same axis (see Fig. 5). Considering a spin valve structure with a hard layer which magnetization unit vector **p** acting as a polarizer and a free layer which magnetization M_S has unit vector **m** ($\mathbf{m} = \boldsymbol{M}/M_S$). The free layer magnetization is affected by various interaction that can be taken into account by defining an effective field (H_{eff}) being given by the sum of all fields: the applied field H, the average dipolar field (H_{dip}) created by the hard layer, the anisotropy field (H_K) created by the magneto-crystalline anisotropy, and the shape anisotropy or demagnetization field $H_{dem} = -M_S$ in the thin film approximation (i.e. the free layer thickness is assumed to be smaller than the nanopillar width):

$$H_{eff} = H - H_{dip} + H_K + H_{dem} \ . \tag{2}$$

The LLGS equation is given by

$$\frac{d\mathbf{m}}{dt} = -\gamma_0 \mathbf{m} \times \boldsymbol{H}_{\mathbf{eff}} + \alpha \mathbf{m} \times \frac{d\mathbf{m}}{dt} - \frac{\beta I g(\theta)}{\gamma_0} \mathbf{m} \times (\mathbf{m} \times \mathbf{p}) \tag{3}$$

where the free layer magnetization dynamics is ruled by three torques: the effective field torque ($\Gamma_{eff} = -\gamma_0 \mathbf{m} \times \boldsymbol{H}_{\mathbf{eff}}$), the damping torque ($\Gamma_{damp} = \alpha \mathbf{m} \times \frac{d\mathbf{m}}{dt}$) and the spin transfer torque ($\Gamma_{STT} = \frac{\beta I g(\theta)}{\gamma_0} \mathbf{m} \times (\mathbf{m} \times \mathbf{p})$) where $\beta = \frac{\hbar \gamma_0}{2\mu_0 M_S V e}$. Where V is the free layer volume, e the elementary charge, $h = 2\pi \times \hbar$ is the Plank's constant, α the damping parameter, $g(\theta)$ the spin transfer efficiency function and with $\gamma_0 = \mu_0 \gamma$ the product of the gyromagnetic ratio γ and the vacuum permeability μ_0.

To determine the stable equilibrium positions of the system, Eq. (3) can be written using an apparent effective field H^*_{eff}

$$\frac{d\mathbf{m}}{dt} = -\gamma_0 \mathbf{m} \times \boldsymbol{H}^*_{\mathbf{eff}} + \alpha \mathbf{m} \times \frac{d\mathbf{m}}{dt} \tag{4}$$

where

$$\boldsymbol{H}^*_{\mathbf{eff}} = \boldsymbol{H}_{\mathbf{eff}} + \frac{\beta I g(\theta)}{\gamma_0} \mathbf{m} \times \mathbf{p} \tag{5}$$

which includes the effective magnetic field and the injected current contributions to the magnetization dynamics. If α is small enough, the damping torque term can be approximated to $\Gamma_{damp} = -\alpha \gamma_0 \mathbf{m} \times (\mathbf{m} \times \boldsymbol{H}_{eff})$.

At equilibrium when $\frac{d\mathbf{m}}{dt}=0$ the magnetization of the free layer is aligned with the effective field H_{eff}^{*}. Therefore, the system of equations giving in spherical coordinates (Fig. 5) the equilibrium positions of the magnetization [86] is

$$\begin{cases} \boldsymbol{H}_{\boldsymbol{eff}}^{*} \cdot \boldsymbol{e}_{\theta} = 0 \\ \boldsymbol{H}_{\boldsymbol{eff}}^{*} \cdot \boldsymbol{e}_{\phi} = 0 \end{cases} \tag{6}$$

To simplify the analytical study of the stability, we will make the assumption that the motion of the magnetization along the $\boldsymbol{e}_{\phi}$ direction is negligible at the onset of reversal. This implies that the magnetization remains close to the perpendicular direction at the equilibrium. Within this approximation, the stability of the equilibrium positions is only determined by the action of the torques exerted on the magnetization along the $\mathbf{e}_{\theta}$ direction.

The stability criterion [86] than can be used is

$$\left[\frac{d}{d\theta}\left(\frac{d\mathbf{m}}{dt}\cdot\mathbf{e}_{\theta}\right)\right]_{\theta=\theta_{eq},\phi=\phi_{eq}} \leq 0 \quad . \tag{7}$$

Moreover, the θ dependence of the g(θ) function will not be taken into account during the derivation but each equilibrium position will be characterized by a different g(θ) value. For instance, g(0) and g(π) will represent the value of the g(θ) function respectively in the parallel and antiparallel states whatever is the angular position of these magnetic configurations.

To determine analytically the state diagram in the case of perpendicular anisotropy, the evolution of the switching currents as a function of the *H* starting from a P or AP state need to be calculated. The switching occurs when these stable equilibrium positions become unstable based on the stability criterion given by Eq. (7). In the following we also consider the hard layer magnetization as fixed and the free layer magnetization as uniform (Fig. 5). Each layer can be modeled as macrospins with uniaxial symmetry. For the case the magneto-crystalline anisotropy axis, the applied magnetic field and the flowing current are along the z direction. Consequently the effective field is along z and derives from the expression of the magnetic energy of the system given by

$$E(\theta,H) = KV\sin^{2}(\theta) - \mu_{0}M_{S}VH\cos\theta \,. \tag{8}$$

The effective field is given by

$$\boldsymbol{H}_{\boldsymbol{eff}} = -\frac{1}{\mu_{0}M_{S}V}\frac{d\boldsymbol{E}}{dm} = (H + H_{K}\cos\theta)\boldsymbol{e}_{z} \tag{9}$$

where $H_{K} = \frac{2K}{\mu_{0}M_{S}}$ and the apparent effective field $\boldsymbol{H}_{\mathbf{eff}}^{*}$ is given by

$$\boldsymbol{H}_{\mathbf{eff}}^{*} = \frac{\beta I g(\theta)}{\gamma_0}\left[(\sin\theta\sin\phi)\boldsymbol{e}_x - (\sin\theta\cos\phi)\boldsymbol{e}_y\right] + (H + H_K\cos\theta)\boldsymbol{e}_z \ . \tag{10}$$

From Eq. 5, the equilibrium positions are the solutions of the following equations:

$$\begin{cases} (H + H_K\cos\theta)\sin\theta = 0 \\ I\sin\theta = 0 \end{cases} . \tag{11}$$

The valid solutions at any injected current corresponds to the exact P or AP magnetic configurations ($\theta = 0$ or π). The stability is determined by the criterion given by

$$\left[(h + g(\theta)i)\cos\theta + \cos(2\theta)\right]_{\theta=0 or \pi} \geq 0 \ . \tag{12}$$

Here, we used reduced coordinates for the applied magnetic field $h = \frac{H}{H_K}$ and for the injected current $i = \frac{\beta I}{\alpha\gamma_0 H_K}$ from the above expression we can deduce that the parallel and the antiparallel states are respectively stable only if the current $I \geq I_{SW}^{P}(H)$ or $I \leq I_{SW}^{AP}(H)$

$$i_{SW}^{P}(h) = -\frac{(h+1)}{g(0)} \quad \Leftrightarrow \quad I_{SW}^{P}(H) = -\left(\frac{2e\mu_0}{\hbar}\right)\frac{\alpha M_S V}{g(0)}(H + H_K) \tag{13}$$

$$i_{SW}^{AP}(h) = -\frac{(h+1)}{g(\pi)} \quad \Leftrightarrow \quad I_{SW}^{AP}(H) = -\left(\frac{2e\mu_0}{\hbar}\right)\frac{\alpha M_S V}{g(\pi)}(H - H_K) \tag{14}$$

The theoretical determination of the switching currents given by Eqs. (13) and (14) allows us to build the state diagram of a nanopillar spin-valve with PMA. The theoretical expressions of the switching currents respectively in the parallel and in the antiparallel states divide the (H, I) plane into two regions, one where the equilibrium position is stable and one where it is unstable based on the stability criterion given by Eq. (7). The border line between these two regions is given by the equation of the switching current evolution as a function of the applied magnetic field. The state diagram of Fig. 6(a) is a combination of the information given by Eqs. (13) and (14). Since the spin-transfer torque is more efficient in the antiparallel configuration than in the parallel one the slopes of the two borders which depend on the g(θ) function are different. So, they cross and divide the (H, I) plane into four regions. In three of them the magnetization has access to at least one stable magnetic configuration: P, AP or both. In the fourth region, there are no stable and static magnetic states. Therefore, the magnetization has to be in a dynamic state where $\frac{d\mathbf{m}}{dt} \neq 0$.

Such theoretical state diagrams have been described in the literature by different methods [24, 50, 87, 88]. A careful analytical study of the fourth region shows that steady magnetization precessions around the perpendicular axis are expected [88].

IV. Experimental results vs the uniaxial model

There are a number of similarities between the theoretical state diagram calculated in this uniaxial approach and the experimental state diagrams (see Fig. 6). Both are composed of two borders dividing the (*H, I*) plane into the same four regions. At high positive field and current, the spin-valve is in the parallel state whereas at high negative field and current it is in the antiparallel state. At high positive field and negative current, it can be either parallel or antiparallel, this is the bistable region characterized by hysteresis loops. At high negative field and positive current it is neither parallel nor antiparallel. From the theoretical results, the field hysteresis loops has to shift toward the negative field when the current increases while its width shrinks. When the two borders cross, the hysteresis loops show a series of differential resistance peaks in the experimental state diagrams.

These peaks are compatible with the magnetization precessions predicted by the theory. Such precessions are commonly recorded in spin-valves with at least one magnetization in-plane because they generate an alternative voltage thanks to the angular dependence of the giant magnetoresistance. However, in these all perpendicular spin-valves, a uniform precession of the magnetization of the free layer around the out-of-plane axis does not affect the angle between the magnetizations of the free layer and of the polarizer. As a consequence, no alternative voltage can be generated in first approximation. These precessions have to be detected indirectly thanks to differential measurements and a lock-in technique. Unfortunately, these methods cannot guarantee that every measured peaks are the consequence of magnetization precessions. Note that another method using GHz Microwave irradiation has been developed to enhance and detect spin-torque driven magnetization precession in nanopillars with magnetic perpendicular anisotropy [55].

The borders determined by the switching fields or currents evolve linearly over a large range of current and field however around the zero current switching fields a strong deviation from this linearity occurs. Experimentally it seems that the magnetization reversal becomes virtually independent of the injected current around these two fields and the current has to reach a critical value before the linear evolution appears. We can then defined a threshold current usually named critical current in the following at which spin transfer torque affect the magnetization switching [6, 86]. This observation seems in contradiction with the theoretical predictions since spin-transfer effect is expected to always modify the damping by increasing or decreasing the impact of the damping torque. The experimental state diagrams in this perpendicular geometry are actually much closer to the state diagrams in the planar geometry than expected (for instance [44-47]).

The initial proposed model is based on a macrospin model with three main hypotheses: there is no thermal activation, the hard and free layers can be modeled by a macrospin and the system is uniaxial. The influence of the hypotheses was tested by looking at the effect of various parameters on the state diagram: temperature (Fig. 7), sweeping rate (Fig. 8), time measurement (Fig. 9), size (Fig. 10) or field orientation (Fig. 11).

In Fig. 7, both temperature (20 K and 300 K) exhibit regions around the zero current switching fields where the current influence on the reversal is weak. However, the absolute values of the critical currents seem to increase when the temperature decreases. The current influence is even weaker at low temperature, consequently, the origin of the critical currents is not thermal activation. This conclusion is confirmed by numerical calculations of the state diagram of a nanopillar spin-valve with perpendicular magnetization by Zhu and Visscher

[56]. In their modeling, they consider the same macrospin model but including temperature which is finite. In this case, they found a theoretical state diagram similar to the one presented in figure 7 with a linear evolution of the switching currents. Note that the reason why the slope of the switching current vs field seems to be changing with temperature remains unclear. This behavior deviates from the macrospin model.

In Fig. 8, we also could test on a different sample the influence of the sweeping rate. Note that this also probes the effect of thermal activation [89, 90]. Again a weak effect of thermal activation on the shape of the state diagram is observed.

A further approach to study the state diagram in the zero-temperature case is to reduce the measurement time. As it is not possible to directly record the phase diagram on the timescale of the magnetization dynamics, a different approach is needed. By determining the switching probability for short current pulses, it is possible to directly study the system on timescales from 100 ps upwards [54]. It is also possible to carry out measurements not only in the thermally excited regime, but also on a short-time regime, in which the switching process is only limited by the angular momentum transfer into the system [91]. For both the thermally as well as the ballistic regime the validity of the macrospin model has been studied and validated, by measuring the switching probabilities switching currents and their field dependence are directly accessible.

It is possible to eliminate the influence of thermal excitations by measuring the switching probabilities on sub-ns timescales and by extrapolating the LLG solution to infinite time, we can thus directly obtain the zero-temperature switching currents as a function of the applied magnetic field [54].

Figure 9 shows the zero-temperature critical switching currents as a function of the applied magnetic field on top of the state diagram measured at room temperature. The boundary defined by the crosses is the limit the state diagram would expand to if it was measured at infinite speed and zero temperature, conversely the room temperature state diagram lies inside and at some distance to the zero-temperature lines. As expected the value of the switching current for short pulses is bigger than in the quasi-static case nevertheless a linear behavior between field and current is observed.

To test the impact of the macrospin approach on the experimental state diagram, Fig. 10 compares the state diagrams obtained for two hexagonal nanopillar spin-valves with different sizes. Note that to compare two state diagrams measured on samples with different sizes, the state diagram are plotted with the current density ($J = I/S$ where S is the area of the nanopillar) instead of the current intensity. Smaller samples are closer to the macrospin approach because it is easier for the exchange interaction to dominate over the demagnetizing field. However, there is no clear evidence of behavior difference between Figs. 10(a) and 10(b). Here, the blue and red slopes can changed from pillar to another due to a slight change of the parameters values (M_S, α…) as well as the dipolar field.

As a result, it is not obvious that introducing a micromagnetic approach into the modeling of the spin-valve will reproduce a much better experimental state diagram. This conclusion is confirmed by the micromagnetic simulation presented in Ref. 50 where it is found a theoretical state diagram close to the analytical state diagram presented.

Nevertheless it is clear that non-uniform magnetization reversal plays an important role in the magnetization reversal processes. Indeed it was shown that the formation of domains and domain walls could be observed [11-13, 92, 93] and that it was influencing the slow magnetization switching dynamics. It influences fast dynamics as well as [54, 55, 91, 92].

The last important hypothesis of our modeling is that all the contributions of the system are along the same axis. This is the uniaxial approximation. To test the impact of the symmetry on the experimental state diagrams, Fig. 11 compares two experimental state diagrams measured on the same elliptical nanopillar spin-valve where the magnetic field is applied in two different directions. In Fig. 11(a), it is applied at 40 deg from the perpendicular direction whereas in Fig 11(b) it is applied close to the perpendicular axis. When the magnetic field is applied away from the perpendicular direction, the effective field has a non-perpendicular component which breaks the uniaxial symmetry. In this case it seems that the field direction is affecting the state diagram.

This conclusion is confirmed by a study of the distortion of the Stoner-Wohlfarth astroid by a spin polarized current of these nanopillar spin-valves [86]. Indeed, it shows that above a critical angle of application of the magnetic field, the injected current has no impact on the magnetization reversal. Therefore, one can state that the experimental state diagrams deviate from our modeling if the uniaxial symmetry is broken. In the section V, we will try to refine our initial modeling by considering a non-uniaxial effective field exerted on the free layer due to the application of a magnetic field away from the perpendicular direction.

V. Non-uniaxial theoretical state diagram

In this non-uniaxial approach, we will use the same modeling as the section III except for the orientation of the applied magnetic field. Here, the field can be applied in the y-z plane at an angle Ψ with the perpendicular direction with $\Psi \in]0,\pi]$ (see Fig. 12).

We will then use the Eq. (6) to obtain the equilibrium positions and the Eq. (7) to study their stability. In order to perform the calculation analytically, we assume that the magnetization is close to the parallel or to the antiparallel configurations at the equilibrium. Even if these conditions are very restrictive, the following analysis shows that they nicely reproduce the behavior of our nanopillar. A more rigorous method of calculation developed by Bazaliy *et al.* can be found [26]. The general aspects of the theoretical state diagram obtained by these two methods are similar.

To calculate the evolution of the switching currents as a function of the applied magnetic field we need first to calculate the expression of the effective field in the framework of this non-uniaxial modeling. According to the description of the system, its magnetic energy is given by

$$E(\theta,H) = KV\sin^2\theta - \mu_0 M_S V \mathbf{m}\cdot\boldsymbol{H} \tag{15}$$

where V is the volume of the free layer. The effective field related to this magnetic energy is given in the basis $(\boldsymbol{e}_x,\boldsymbol{e}_y,\boldsymbol{e}_z)$ by

$$\boldsymbol{H}_{eff} = (H\sin\Psi)\boldsymbol{e}_y + (H\cos\Psi + H_K\cos\theta)\boldsymbol{e}_z . \tag{16}$$

The dipolar coupling and the demagnetizing field are not taken into account. In the basis ($\boldsymbol{e}_x$, $\boldsymbol{e}_y$, $\boldsymbol{e}_z$) we still have $\mathbf{m}\times\mathbf{p} = (\sin\theta\sin\varphi)\boldsymbol{e}_x - (\sin\theta\cos\varphi)\boldsymbol{e}_y$ As a result, the apparent effective field is given by

$$\boldsymbol{H}_{eff}^{*} = \frac{\beta I g(\theta)}{\gamma_0}\left[(\sin\theta\sin\phi)\boldsymbol{e}_x - (\sin\theta\cos\phi)\boldsymbol{e}_y\right] + (H\sin\Psi)\boldsymbol{e}_y + (H\cos\Psi + H_K\cos\theta)\boldsymbol{e}_z . \quad (17)$$

Therefore, from Eq. (6) the equilibrium positions are the solutions of the following system

$$\begin{cases} (H\cos\Psi + H_K\cos\theta)\sin\theta = H\sin\Psi\cos\theta\sin\phi \\ \beta I g(\theta)\sin\theta = \gamma_0 H\sin\Psi\cos\phi \end{cases} . \quad (18)$$

The stability of these equilibrium positions is determined by the criterion given by Eq. (7). Here, we have

$$\frac{d\mathbf{m}}{dt}\cdot\boldsymbol{e}_\theta = -\left[\alpha\gamma_0(H\cos\Psi + H_K\cos\theta) + \frac{\beta I g(\theta)}{\gamma_0}\right]\sin\theta + \alpha\gamma_0 H\sin\Psi\cos\theta\sin\phi + H\sin\Psi\cos\phi . \quad (19)$$

With the assumption that the movement of the magnetization along the $\boldsymbol{e}_\phi$ direction is negligible from the reversal point of view the stability criterion in this non-uniaxial modeling becomes

$$\left[(h\cos\Psi + g(\theta)i)\cos\theta + h\sin\Psi\sin\theta\sin\phi + \cos(2\theta)\right]_{\theta=\theta_{eq};\phi=\phi_{eq}} \geq 0 . \quad (20)$$

The θ dependence of the $g(\theta)$ function will not be taken into account during the derivation. To solve analytically these equations we will consider by analogy with the previous modeling that the magnetization can be into two opposite magnetization configurations: one close to the parallel state where $\theta \approx 0$ and $\phi \approx \frac{\pi}{2}$ and one close to the antiparallel state where $\theta \approx \pi$ and $\phi \approx -\frac{\pi}{2}$. As a result, the movement of the magnetization along the $\boldsymbol{e}_\phi$ direction is indeed negligible from the reversal point of view.

If we consider the case of a parallel to antiparallel switching ($\theta \approx 0$ and $\phi \approx \frac{\pi}{2}$) and in first order approximation the set of Eq. (18) gives the following coordinates for the equilibrium position

$$\theta_{eq} = \frac{h\sin\Psi}{h\cos\Psi + 1} \quad (21)$$

$$\phi_{eq} = \frac{\pi}{2} - \frac{\alpha g(\theta) i}{h\cos\Psi + 1} . \quad (22)$$

Here, contrary to the purely uniaxial case, the position of the magnetization of the free layer at the equilibrium evolves as a function of the applied magnetic field. Moreover, it is not contained in the y-z plane because of the action of the spin transfer torque.

In first order approximation and injecting the θ_{eq} value of the equilibrium position of Eq. (21) the stability criterion given by the Eq. (20) becomes for the parallel magnetic configuration

$$h^2 + \left[\left(g(0)i + 2\right)\cos\Psi\right]h + g(0)i + 1 \geq 0 \ . \tag{23}$$

Therefore, in this non-uniaxial modeling, the region of the (*H, I*) plane where the parallel magnetic configuration is stable is given by the following expression of the switching current as a function of the applied magnetic field

$$i \geq -\frac{h^2 + 2h\cos\Psi + 1}{g(0)\left(h\cos\Psi + 1\right)} \ . \tag{24}$$

In the non-uniaxial case ($\Psi \neq 0$), the evolution of the switching current is represented on Fig. 13 (called here stability diagram). A vertical asymptote at $h = -\frac{1}{\cos\Psi}$ divides the curve into two branches. If $h < -\frac{1}{\cos\Psi}$ the switching current decreases with the applied magnetic field until it reaches a minimum value at $h = -\frac{1+\sin\Psi}{\cos\Psi}$. If $h > -\frac{1}{\cos\Psi}$ the switching current increases with the applied magnetic field until it reaches a maximum value $h = -\frac{1-\sin\Psi}{\cos\Psi}$. The expressions of this local minimum and of this local maximum of the switching current are respectively given by

$$i_{\min}^{P} = \frac{2}{g(0)}\left(\frac{\sin^2\Psi + \sin\Psi}{\cos^2\Psi}\right) \tag{25}$$

$$i_{\max}^{P} = \frac{2}{g(0)}\left(\frac{\sin^2\Psi - \sin\Psi}{\cos^2\Psi}\right). \tag{26}$$

When the injected current ranges between these two values, the stability diagram of the parallel magnetic configuration shows that the parallel state becomes unstable for a constant applied magnetic field $h = -\frac{1}{\cos\Psi}$ (see Fig. 13(a)). Therefore, in this region the spin-transfer torque does not affect the stability of the parallel state. It has to reach the $i_{\min}^{P}$ or $i_{\max}^{P}$ value depending on its sign to have an impact on the parallel to antiparallel reversal. These values correspond to the critical currents highlighted in the experimental state diagrams. Outside these critical currents, the evolution of the switching currents tends to be linear and close to the evolution predicted by the uniaxial model.

Similarly for the antiparallel to parallel switching ($\theta \approx \pi$ and $\phi \approx -\frac{\pi}{2}$), in the non-uniaxial case ($\Psi \neq 0$):

$$i \leq -\frac{h^2 - 2h\cos\Psi + 1}{g(\pi)(h\cos\Psi - 1)} \tag{27}$$

and

$$i_{\min}^{AP} = -\frac{2}{g(\pi)}\left(\frac{\sin^2\Psi + \sin\Psi}{\cos^2\Psi}\right) \tag{28}$$

$$i_{\max}^{AP} = -\frac{2}{g(\pi)}\left(\frac{\sin^2\Psi - \sin\Psi}{\cos^2\Psi}\right) \tag{29}$$

The evolution of the switching current as a function of h is then represented on Fig. 13(b) and is very similar to the parallel to antiparallel switching. One could then deduced the expression of the switching current as shown in Table I for both the pure out of plane and in-plane anisotropy. The calculation could be done either by performing a stability analysis [26, 44] or by using a power dissipation approach as in [6].

The theoretical determination of the switching currents given by Eqs. (24) and (27) allows us to draw a theoretical state diagram of a nanopillar spin-valve with perpendicular magnetizations in this non-uniaxial approach. Figure 14(a) presents the theoretical state diagram obtained in this non-uniaxial approach. Contrary to the uniaxial modeling where the evolution of the switching current is always linear (see Fig. 6(a)), in this modeling the quasi-linear evolution of the switching current is broken between critical current values (see Fig. 14(b)). Between these critical currents, the reversal of the magnetization does not depend on the injected current. Indeed, the switching field remains constant at its value when there is no injected current. This non-uniaxial modeling gives a closer description of the experimental observations (see Fig. 6(b)).

Therefore, it seems that the breaking of the uniaxial symmetry of the spin-valve with perpendicular magnetizations is the key parameter to understand the shape of the state diagrams in this system. In the next section, we shall search for the experimental reason that can justify such a break in the uniaxial symmetry.

VI. Origin of the symmetry breaking

The origin of the non-uniaxiality can either be extrinsic as a misaligned magnetic field or intrinsic as a deviation of the free layer easy axis. Those two hypothesizes have been tested by computing the LLGS equation (Eq. (2)).

The following simulations have been realized with our own software solving LLGS equation (Eq. (3)) with the Cash-Karp method [94]. The scalar function $g(\theta)$ in the spin transfer torque takes the form given by Slonczewski [4]. The state diagrams are computed in the macrospin approximation at zero-temperature. The calculations are done taking into account the average dipolar fields resulting from a spin-valve structure with two magnetic layers having a

rectangular shape 50 nm by 100nm. The free layer characteristics were chosen close to the experimental values, hence the damping constant $\alpha = 0.25$, the anisotropy constant $K = 3\times10^5\ J/m^3$, the saturation magnetization $M_S = 6.5\times10^5\ kA/m$, the thickness of 1.8 nm and the polarization equals 0.28. The hard layer magnetization is supposed fixed along the z axis (see Fig. 5).

The theoretical state diagram calculated in the uniaxial case is shown in Fig. 15. This simulated state diagram resembles to the theoretical one (see Fig. 6(a)) calculated with the analytical model in the uniaxial approach.

Figures 16 exhibits two simulated state diagrams where the magnetic field is tilted with an angle Ψ from the perpendicular direction (see Fig. 12). A critical current i.e the deviation to the linearity of the switching current appears clearly for a tilted angle of $\Psi = 5^\circ$ (see Fig. 16(a)). The values of the critical currents extend increases when the tilted angle Ψ increases (see Fig. 16(b) for $\Psi = 20^\circ$).

The influence of the misaligned easy anisotropy axis defined by Ψ_{ani} the angle between the easy axis anisotropy and the perpendicular direction is shown on the Fig. 17. For $\Psi_{ani} \neq 0^\circ$, the state diagram exhibits a part where the reversal of the magnetization does not depend on the current. The presence of a critical current is similar to the previous simulations with a tilted magnetic field (Fig. 16). However, the influence of the anisotropy angle is much stronger than the applied magnetic field. So a slight misalignment of the anisotropy axis has a greater influence than the magnetic field on the magnetization reversal. We verified that in our experiments the field was not misaligned by an angle larger than one degree. We can therefore conclude that applied field misalignment is not playing a major role in the shape of the experimental state diagram.

Finally we considered the effect of a second ordered anisotropy constant value K_2. We assumed a sample with a weak in plane anisotropy component K_p corresponding to the in-plane shape anisotropy. The presence of K_p induced a weak breaking on the uniaxial symmetry. The Fig. 18 compares two computed states diagrams without (Fig 18(a)) and with the taking into account K_2 (Fig 18(b)). The value of $K_2 = 1\times10^5\ J/m^3$ is chosen to be 1/3 of K . We notice an increase of the critical current due to K_2 . For Figs. 18(a) and 18(b), the anisotropy constants sum ($K_1 + K_2$) is kept constant.

An energetic analysis of the system is required to explain this behavior. The expression of the magnetic energy of the system is given by

$$E(\theta, H) = K_1 V \sin^2(\theta) + K_2 V \sin^4(\theta) + K_p V \cos^2(\theta) - \frac{1}{2}\mu_0 V M_S \sin^2(\theta) - \mu_0 M_S V H \cos\theta \quad (30)$$

where θ is the angle between the perpendicular axis and the magnetization of the free layer. The first 3 terms in Eq. (30) are related to the first-order, second-order and in plane anisotropy contribution respectively, the fourth and the fifth terms are respectively the demagnetizing and the Zeeman energy. Using Eq. (30), we can calculate the energy landscape of the system as a function θ (Fig. 19). The investigation of the equilibrium positions, at the extremum of energy, gives us the static or dynamic configuration of the system respectively [6]. In Fig. 19,

we observe for the curve with $K_2 = 1\times10^5\ J/m^3$ (green curve), for an applied field of 200mT close to the H_K value, the presence of one potential well at $\theta = 0$ (the parallel state) and two other stable state close to $\theta = \pi$. As a result, other stable states are now available. Since those two new states are not aligned with the anisotropy axis, it leads to a symmetry breaking.

We have then demonstrated that several factors lead to a symmetry breaking that can explain the experimental state diagram. Since it is unlikely that for all experiments the applied field is strongly misaligned we then suspect that the magnetocrystalline anisotropy plays an important role. Indeed a misalignment of the anisotropy axis with the current flow is probable. To verify this point, an experimental study on an epitaxial crystalline [Co/Ni] system with a well-definedanisotropy axis [95] is underway. Moreover because of the presence of grains in the sputtered sample one can expect a distribution of anisotropy axis for each nanopillar. Finally since a pure hexagonal Co shows at RT a second-order anisotropy constant value K_2 (1.44×10^5 J/m^3) close to first-order one K_1 (4.53×10^5 J/m^3) [96], Co-based alloys as [Co/Ni] and [Co/Pt] layers are expected to exhibit a similar behavior. It is then likely that the materials used have strong second-order anisotropy constant that enhance the symmetry breaking which is responsible for the measured experimental state diagram. Note that theses materials with a strong K_2 are also of great interest in magnetic recording media since higher thermal stability can be achieved [97, 98] for a given reversal field. In the future it is then of great interest to continue the characterization and the study of the origin of perpendicular magnetic anisotropy in thin film and multilayers [99-101].

VII. Conclusion

In this paper, we have studied the magnetic state of nanopillar spin-valves with strong perpendicular anisotropy. We showed that the magnetic states of the layers depend on the applied magnetic field and the DC current injected to the device and that consequently maping the magnetic states of the system on a comprehensive state diagram is very convenient. The method to build and to interpret the experimental state diagram is explained. The influence of several parameters such as lateral size of the sample, temperature, sweeping field rate, time measurement and field orientation on experimental state diagrams is presented. Analytically the state diagram in a purely uniaxial system is modeled and it is demonstrated that this simple model does not properly reflect the experimental results. It is shown that if the uniaxial symmetry is broken a region for which the current has no effect on the switching can be evidenced as observed experimentally. We finally discussed the possible origins of the symmetry break using an analytical model and numerical simulations. A misalignment of the applied field, anisotropy axis or the presence of strong 2nd order anisotropy constant could explain the experimental results. Future experimental studies are needed to determine the microscopic origin(s) of the symmetry breaking. The complete study conducted here is crucial to describe the magnetization reversal driven by spin transfer torque in model systems. Moreover the discrepancy between uniaxial theory and real device as well as the influence of extrinsic and intrinsic parameters on state diagrams are essential to design proper material for STT-MRAM applications. To ensure a good reproducibility of the switching current and the angular distribution of the anisotropy axis from one grain to the other, studies on epitaxial multilayer system with well-controlled PMA are in progress [95].

Acknowledgement

We thank very much S. Suire for his technical support with transport measurements experiments. This work was supported by The Partner University Fund “Novel Magnetic Materials for Spin Torque Physics and Devices”, NSF Award No. DMR-1008654 and the ANR-10-BLAN-1005 “Friends”.

Captions (Table and Figures)

TABLE I. Comparison between the effective magnetic field ($H_{eff}^{P\to AP}$, $H_{eff}^{AP\to P}$), the energy barrier between the two stable magnetic states (U_K) and the switching current (I_{SW}) of spin-valves with in-plane (i.e anisotropy field in-plane H_{K-ip}) and out-of-plane anisotropy (i.e anisotropy field perpendicular H_{K-oop}). The sketch in figure 1 shows (a) the in plane and (b) the out of plane cases.

FIG. 1. (Color online) Sketch of (a) in plane and (b) out of plane: the polarizer in blue has its magnetization fixed whereas the free layer in green can align parallel of antiparallel to it.

FIG. 2. (Color online) (a) Ac- resistance variation as a function of the net applied magnetic field (H_{net}) under zero current for an elliptical nanopillar spin-valve of 50 nm by 300 nm with a hard layer made of [Co/Pt]/[Co/Ni] and a free layer made of [Co/Ni] with a platinum layer on top. The net applied field is define as the applied field minus the average dipolar field coming from the hard layer ($H_{net=}$ H-H_{dip}). The red and blue curves correspond to the field increasing and decreasing branches of the hysteresis loop. (b) Corresponding difference of the normalized resistances between the field increasing and decreasing branches of the hysteresis loop. (c) Corresponding half sum of the normalized resistances between the field increasing and decreasing branches of the hysteresis loop. The normalized resistances (R-R_P) /(R_{AP}-R_P) are plotted to remove the Joule heating contribution for the R_{sum} curve. These curves highlight three regions of different available magnetic configurations: the parallel (P) or the antiparallel (AP) states only or the bistable region.

FIG 3. (Color online) State diagrams of an elliptical nanopillar spin-valve of 50 nm by 300 nm with a hard layer made of [Co/Pt]/[Co/Ni] and a free layer made of [Co/Ni] with a platinum layer on top obtained (a) from the difference of AC resistances treatment and (b) from the half sum of the AC resistances treatment. The applied magnetic field step is of 1 mT and the injected current step is of 0.1 mA. Data acquired at a sample ambient temperature unless otherwise specified. The colored scale bar corresponds to the value of the normalized resistance for both AC resistances treatment. Note that the same scale bars are used in the following.

FIG. 4. (Color online) State diagram of an elliptical nanopillar spin-valve of 50 nm by 300 nm with a hard layer made of [Co/Pt]/[Co/Ni] and a free layer made of [Co/Ni] obtained from the half sum method along with three characteristic hysteresis loops at I = −13 mA, I = 0 mA and I = 11 mA.

FIG. 5. (Color online) Orientation of the magnetization unit vectors **m** and **p**, applied field **H** and injected current I relative to x,y,z axis in the case of a purely uniaxial symmetry.

FIG. 6. (Color online) (a) Theoretical state diagram of a nanopillar spin-valve with perpendicular magnetizations in the case of a uniaxial, macrospin and 0 K approach in reduced coordinates ($h = \frac{H}{H_K}$ and $i = \frac{\beta I}{\alpha \gamma_0 H_K}$). (b) Experimental state diagram of a hexagonal nanopillar spin-valve of 100 nm by 200 nm with a hard layer made of [Co/Pt]/[Co/Ni] and a free layer made of [Co/Ni]. The blue and red circles are for the measured switching fields and the orange triangle indicate the presence of a peak in the differential resistance measurements. The blue and red lines present what could correspond to the expected evolution of the switching current as a function of the applied magnetic field of our simple modeling. The values of the parameters used here can be found in Ref. 50.

FIG. 7. (Color online) Experimental state diagrams of an hexagonal nanopillar spin-valve of 100 nm by 200 nm with a hard layer made of [Co/Pt]/[Co/Ni] and a free layer made of [Co/Ni] measured at (a) T = 290 K and at (b) T = 20 K. The blue and red lines present what could correspond to the expected linear evolution of the switching current as a function of the applied magnetic field.

FIG. 8. (Color online) Experimental state diagram of an elliptical nanopillar spin-valve of 50 nm by 300 nm with a hard layer made of [Co/Pt]/[Co/Ni] and a free layer made of [Co/Ni] for various sweeping rate of 100mT (background and black line), 10mT/s (red line) and 1T/s (blue line).

FIG. 9. (Color online) Experimental state diagram of a rectangular 100 nm by 100 nm spin valve with a hard layer made of [Co/Pt]/[Co/Ni] and a free layer made of [Co/Ni]. Blue and red correspond to the parallel or antiparallel states. The symbols (cross) indicate the zero temperature switching current extrapolated from short-time measurements [91]. As this extrapolation eliminates the thermal excitations, the switching current significantly is larger than during the quasistatic measurement.

FIG. 10. (Color online) Experimental state diagrams of an hexagonal nanopillar spin-valve with a hard layer made of [Co/Pt]/[Co/Ni] and a free layer made of [Co/Ni] of (a) 100 nm by 200 nm and of (b) 50 nm by 100 nm. The blue and red lines present what could correspond to the expected evolution of the switching current as a function of the applied magnetic field of our simple modeling.

FIG. 11. (Color online) Experimental state diagrams of an elliptical nanopillar spin-valve of 50 nm by 300 nm with a hard layer made of [Co/Pt]/[Co/Ni] and a free layer made of [Co/Ni]. The magnetic field is applied at an angle Ψ toward the perpendicular axis. (a) $\Psi = 40°$ and (b) $\Psi = 0°$. The blue and the red lines present what could correspond to the expected evolution of the switching current as a function of the applied magnetic field of our simple modeling.

FIG. 12. (Color online) Orientation of the magnetization unit vectors **m** and **p**, applied field **H** and injected current I relative to x,y,z axis in the case of a non-uniaxial symmetry.

FIG. 13. (Color online) Stability diagrams in the applied magnetic field and injected current plane in reduced coordinates. The colored areas correspond to the unstable regions and the lines to the theoretical evolution of the switching currents with the applied magnetic field. (a) Case of the parallel state. (b) Case of the antiparallel state.

FIG. 14. (Color online) (a) Theoretical state diagram of a nanopillar spin-valve with perpendicular magnetizations in the case of a non-uniaxial (Ψ = 20°), macrospin and 0 K approach. (b) Theoretical evolution of the critical currents as a function of the angle of application of the magnetic field.

FIG. 15. (Color online) Theoretical state diagram for uniaxial system calculated using numerical simulations. The new reduced coordinates $h = \frac{H}{H_K}$ (bottom) and $i = \frac{\beta I}{\alpha \gamma_0 H_K}$ (right) have been added using the new parameters (see text).

FIG. 16. (Color online) Theoretical state diagrams in the case of a tilted applied field of (a) $\Psi = 5^\circ$ and (b) $\Psi = 20^\circ$.

FIG. 17. (Color online) Theoretical state diagrams in the case of a tilted anisotropy field of (a) $\Psi_{\text{ani}} = 0.5^\circ$ and (b) $\Psi_{\text{ani}} = 5^\circ$.

FIG. 18. (Color online) Theoretical state diagrams in the case with an added in plane $K_p = 1\times10^4\ J/m^3$ and 2nd order K_2 anisotropy constant. (a) $K = K_1 = 4\times10^5\ J/m^3$ and (b) $K_1 = 3\times10^5\ J/m^3$, $K_2 = 1\times10^5\ J/m^3$. The value of the total anisotropy constant K is chosen to be the same in both cases.

FIG. 19. (Color online) Energy landscape of the free layer as a function of the angle θ, for an applied field of 200mT and without injected current. The parameters used here are $K_p = 1\times10^4\ J/m^3$, $K_1 = 3\times10^5\ J/m^3$. The red curve is plotted for $K_2 = 0$, the green one for $K_2 = 1\times10^5\ J/m^3$.

Table and Figures

	In plane	Out of plane
$H_{eff}^{P\to AP}$	$H + H_{dip} + H_{K-ip} + \frac{1}{2}M_S$	$H + H_{dip} + \left(H_{K-oop} - M_S\right)$
$H_{eff}^{AP\to P}$	$-\left(H + H_{dip}\right) + H_{K-ip} + \frac{1}{2}M_S$	$-\left(H + H_{dip}\right) + \left(H_{K-oop} - M_S\right)$
U_K	$\mu_0\left(M_s V H_{K-ip}\right)/2$	$\mu_0\left(M_s V\left(H_{K-oop} - M_S\right)\right)/2$
$\left\|\mathbf{I}_{SW}\right\|$	$\left(\frac{2e}{\hbar}\right)\frac{2\alpha}{g(\theta)p}\left(U_K + \frac{1}{2}\mu_0 {M_S}^2 V\right)$	$\left(\frac{2e}{\hbar}\right)\frac{2\alpha}{g(\theta)p}\left(U_K\right)$

Table I

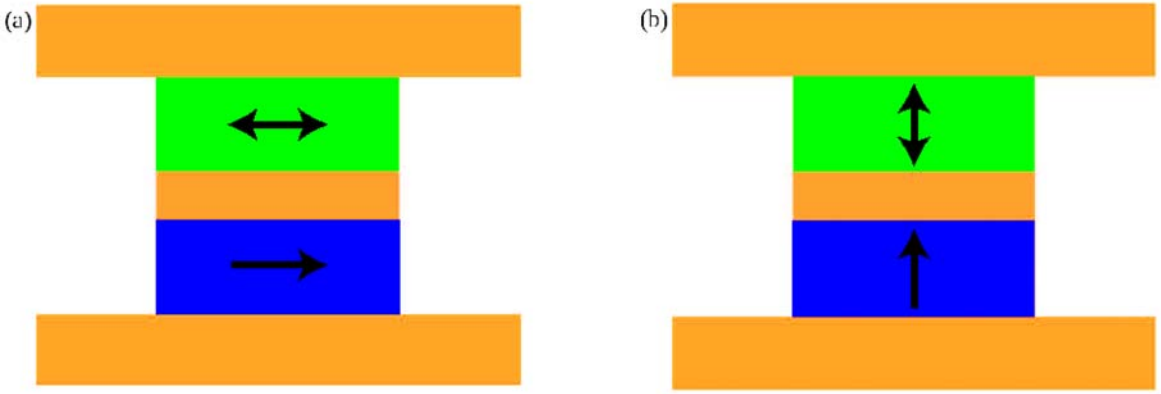

Figure 1

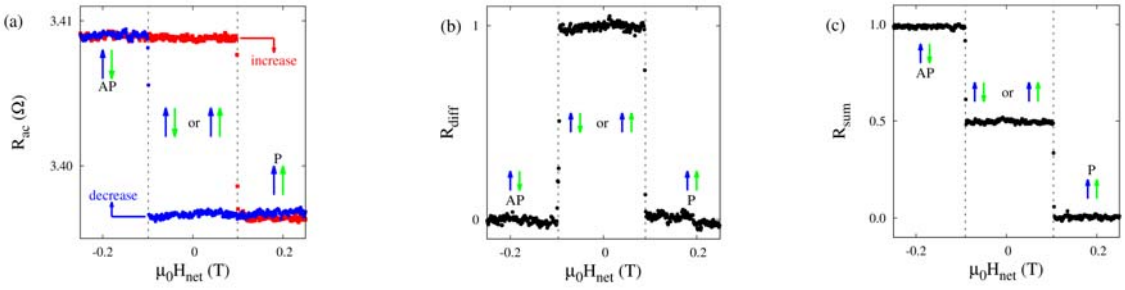

Figure 2

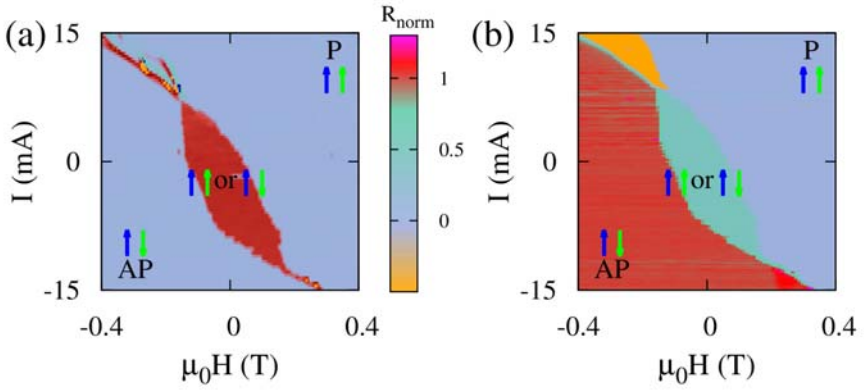

Figure 3

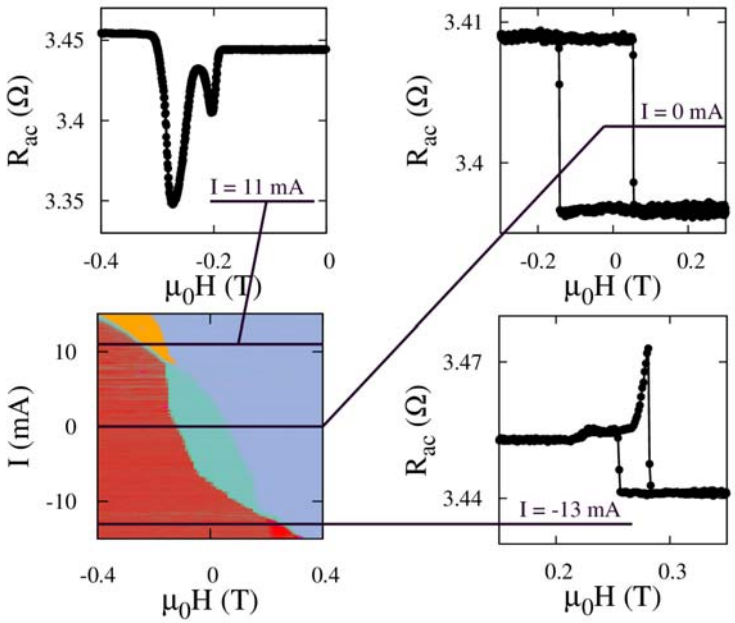

Figure 4

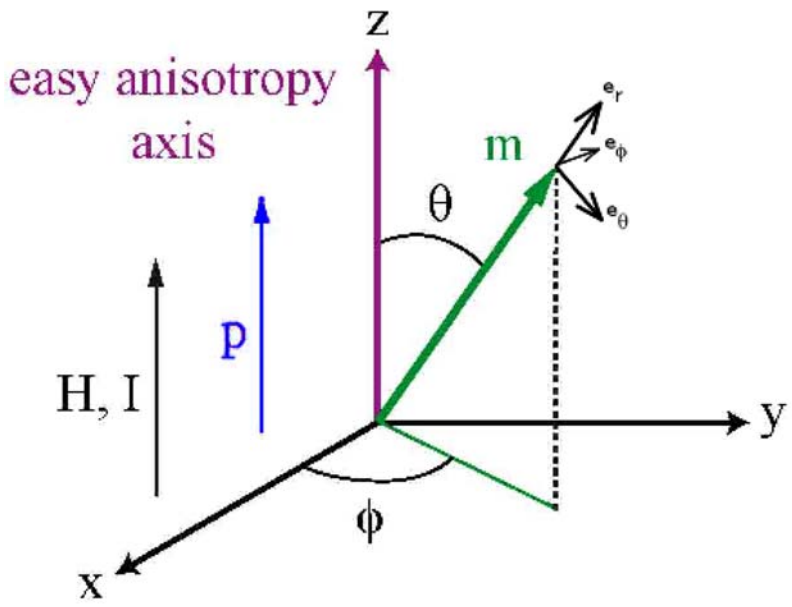

Figure 5

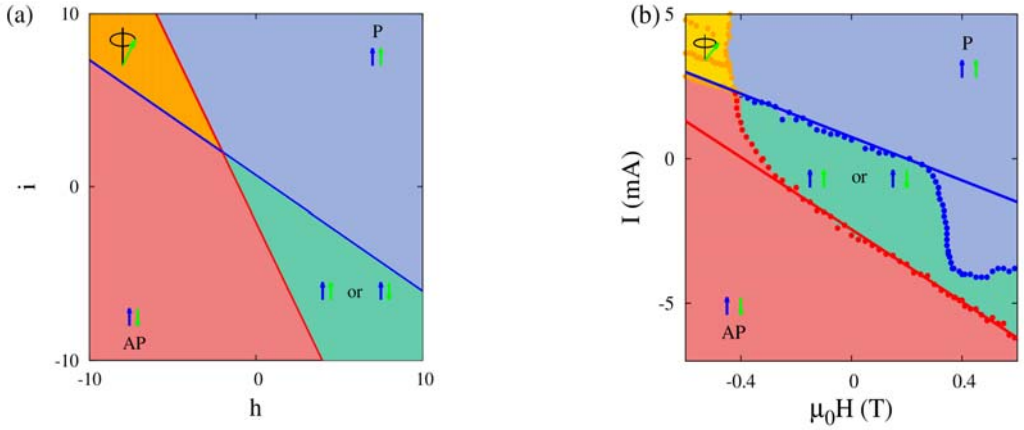

Figure 6

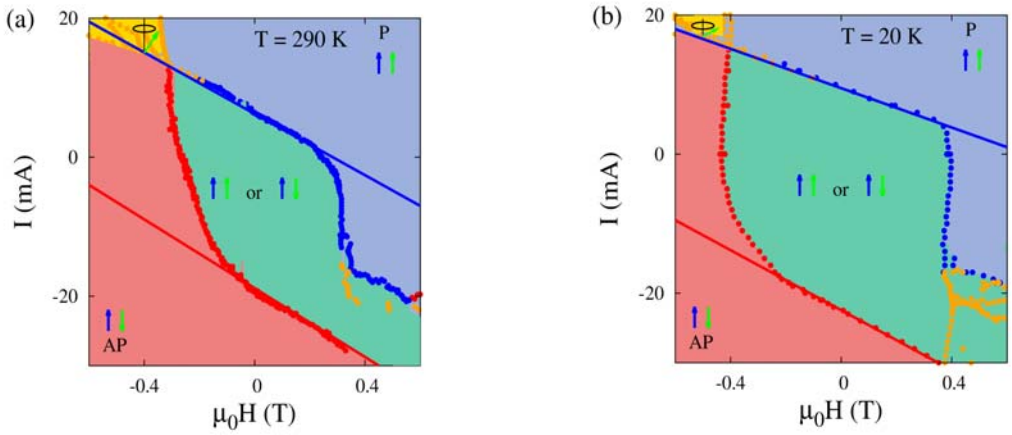

Figure 7

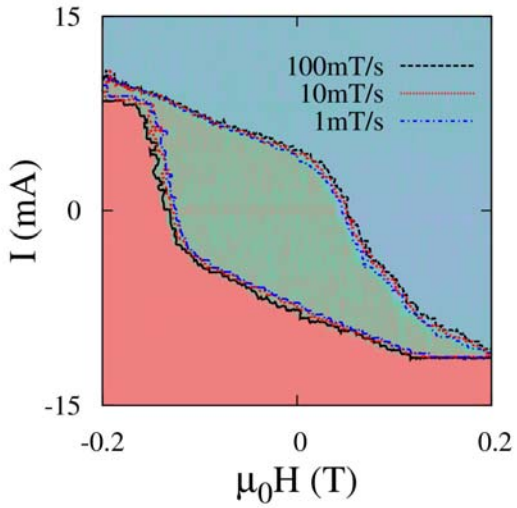

Figure 8

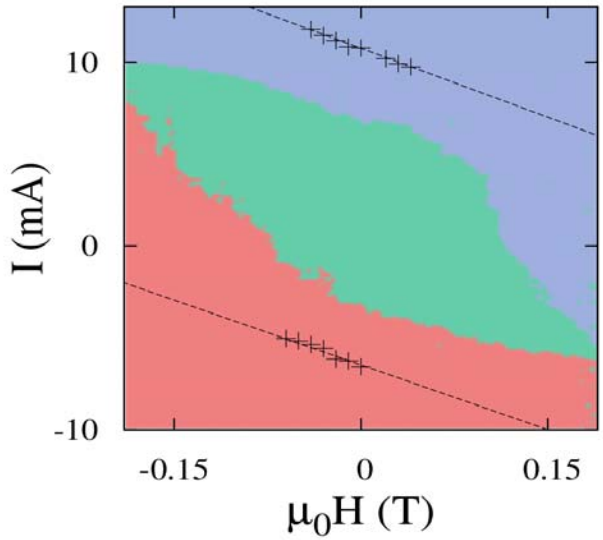

Figure 9

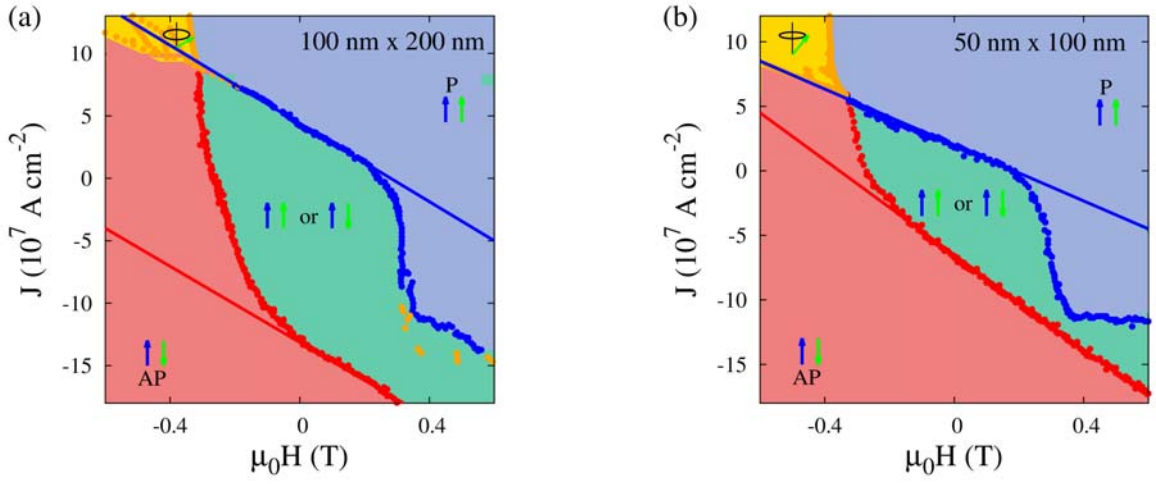

Figure 10

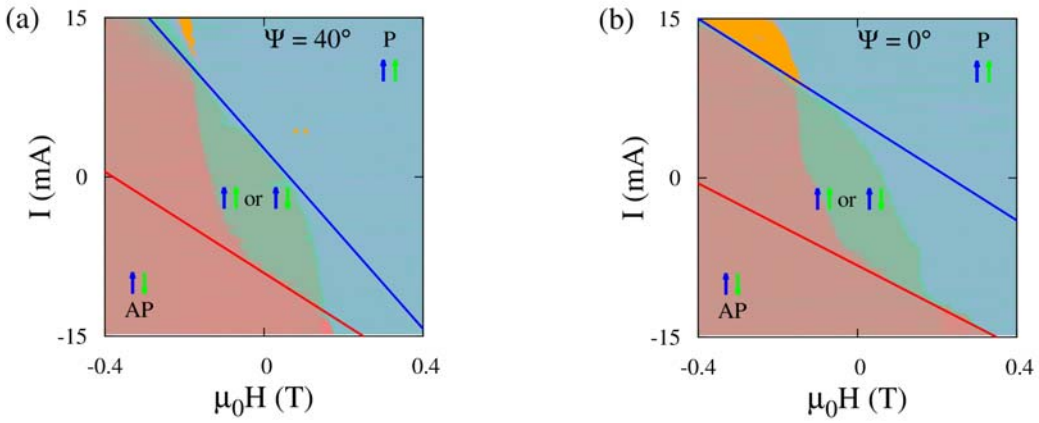

Figure 11

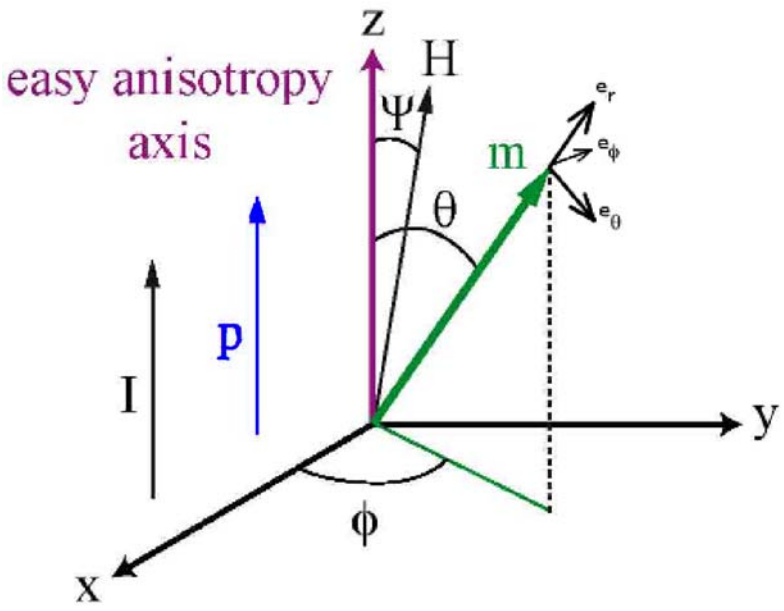

Figure 12

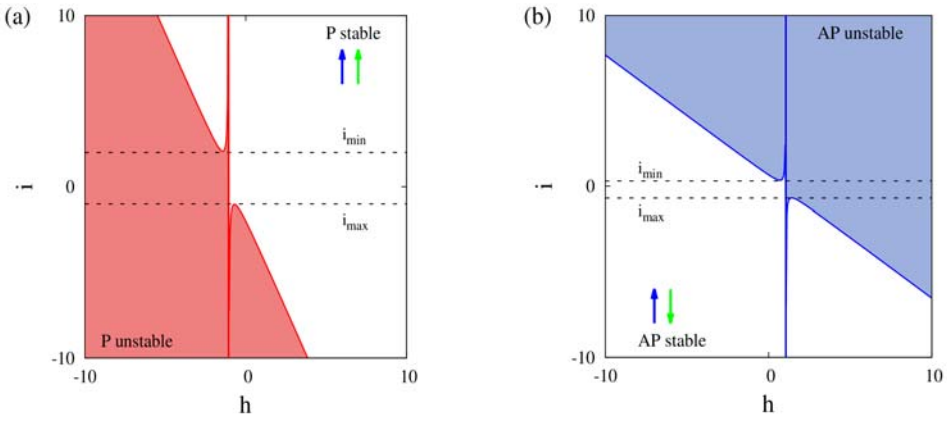

Figure 13

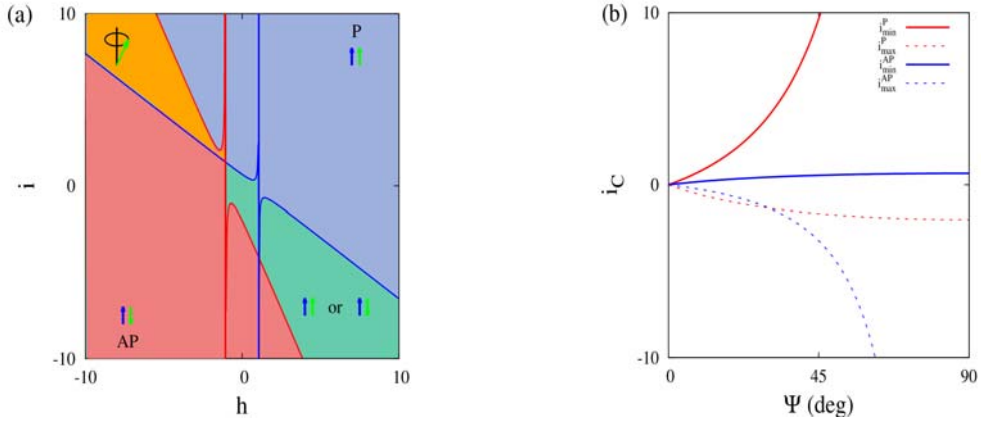

Figure 14

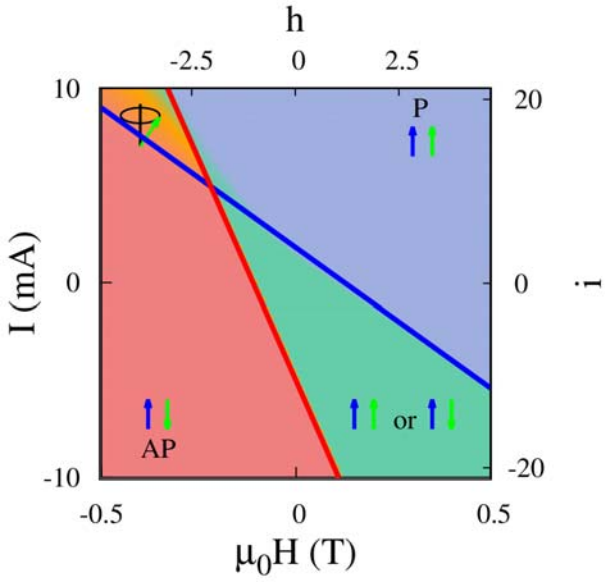

Figure 15

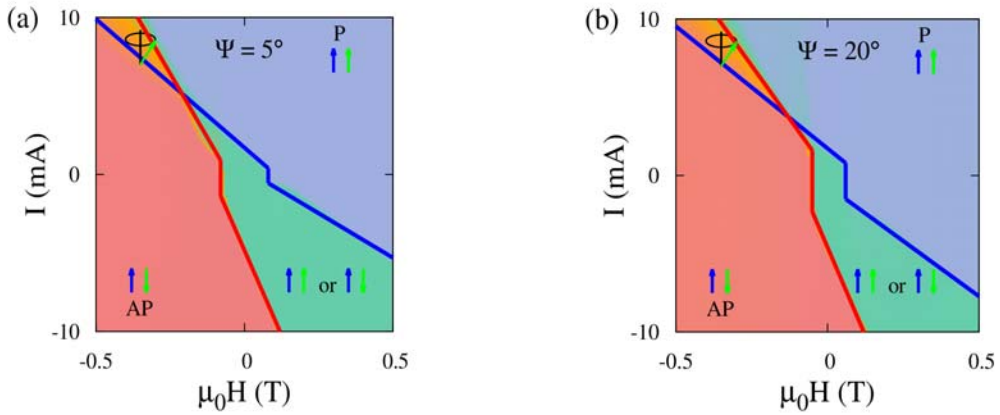

Figure 16

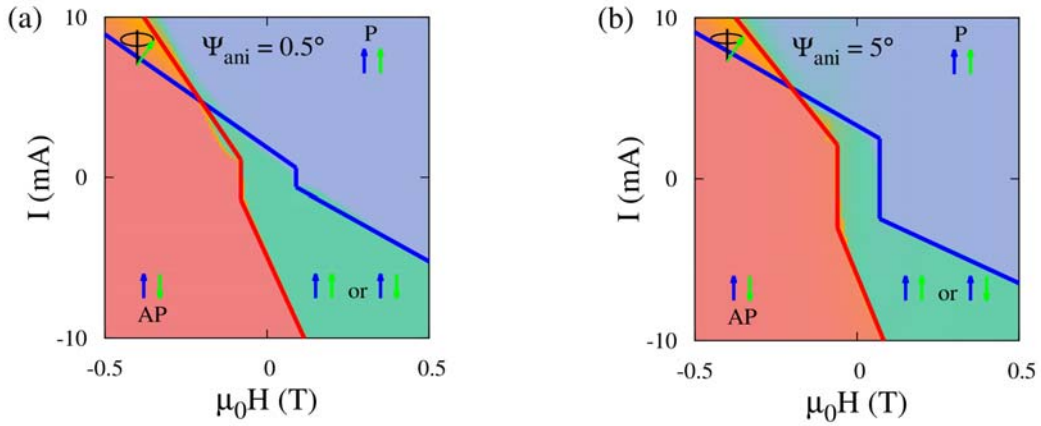

Figure 17

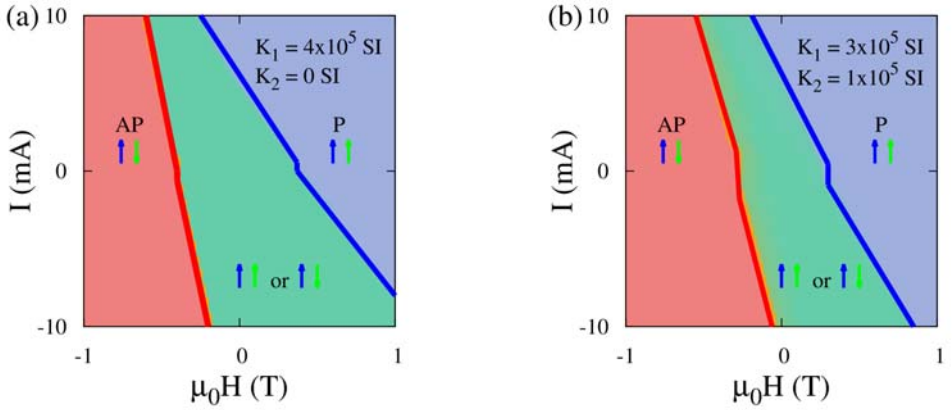

Figure 18

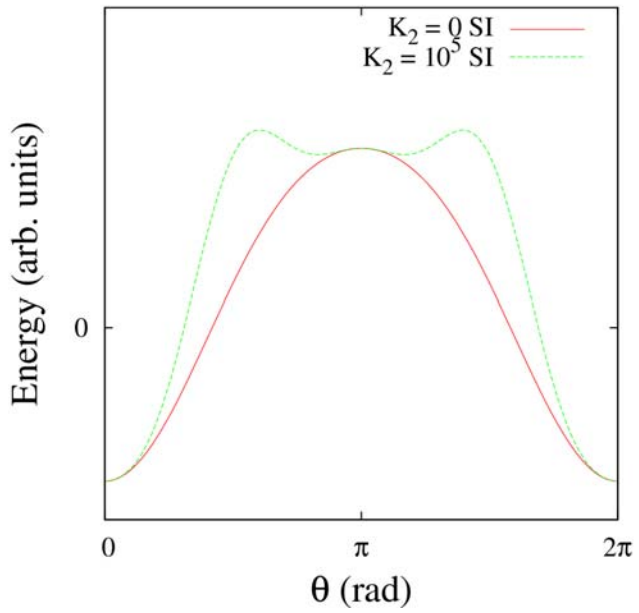

Figure 19

References

[1] L. Berger, J. Appl. Phys. **49**, 2156 (1978)
[2] L. Berger, J. Appl. Phys. **50** 2137 (1979)
[3] L. Berger, Phys. Rev. B **54**, 9353 (1996)
[4] J. C. Slonczewski, J. Magn. Magn. Mater. **159**, L1 (1996)
[5] Ya. B. Bazaliy, B. A. Jones, and S. C. Zhang, Phys. Rev. B **57**, R3213 (1998)
[6] J. Cucchiara, Eric E. Fullerton, A. D. Kent, J. Z. Sun, Y. Henry and S. Mangin, Phys. Rev. B **84**, 100405(R) (2011)
[7] M. D. Stiles, J. Miltat, Spin Dynamics in Confined Magnetic Structures III, edt. by B. Hillebrands and A. Thiaville, Topics in Applied Physics **101**, 225 (2006)
[8] Series of review articles: D. C. Ralph, M. D. Stiles, J. Magn. Magn. Mater. **320**, 1190 (2008); J. A. Katine, E. E. Fullerton, *ibid.*, p. 1217; J. Z. Sun, D. C. Ralph, *ibid.*, p. 1227; D. V. Berkov, J. Miltat, *ibid.*, p. 1238; T. J. Silva, W. H. Rippard, *ibid.*, p. 1260; G. S. D. Beach, M. Tsoi, J. L. Erskine, *ibid.*, p. 1272; Y. Tserkovnyak, A.Brataas, G. E. W. Bauer, *ibid.*, p. 1282; H. Ohno, T. Dietl, *ibid.*, p. 1293; P. M. Haney, R. A. Duine, A. S. Nunez, A. H. MacDonald, *ibid.*, p. 1300
[9] C. H. Marrows, Adv. Phys. **54**, 585 (2005)
[10] P. P. Freitas, L. Berger, J. Appl. Phys. **57**, 1266 (1985)
[11] D. Ravelosona, S. Mangin, Y. Lemaho, J. A. Katine, B. Terris, Eric. E. Fullerton, Phys. Rev. Lett **96**, 186604 (2006)
[12] D. Ravelosona, S. Mangin, J. A. Katine, Eric Eric E. Fullerton, B. D. Terris, Appl. Phys. Lett. **90**, 072508 (2007)
[13] C. Burrowes, D. Ravelosona, C. Chappert, S. Mangin, Eric E. Fullerton, J. A. Katine, and B. D. Terris, Appl. Phys. Lett. **93**, 172513 (2008)
[14] S. S. P. Parkin, M. Hayashi, and L. Thomas, Science **320**, 190 (2008)
[15] M. Tsoi, A. G. M. Jansen, J. Bass, W-C. Chiang, M. Seck, V. Tsoi, and P. Wyder, Phys. Rev. Lett **80**, 4281 (1998)
[16] J. Z. Sun, J. Magn. Magn. Mater. **202**, 157 (1999)
[17] J. A. Katine, F. J. Albert, R. A. Buhrman, E. B. Myers, D. C. Ralph, Phys. Rev. Lett. **84**, 3149 (2000)
[18] S. I. Kiselev, J. C. Sankey, I. N. Krivorotov, N. C. Emley, R. J. Schoelkopf, R. A. Buhrman, and D. C. Ralph, Nature **425**, 380 (2003)
[19] W. Rippard, M. Pufall, S. Kaka, S. Russek, T. Silva, Phys. Rev. Lett. **92**, 027201 (2004)
[20] A. D. Kent, Nature Mat. **6**, 399 (2007)
[21] J. A. Katine and Eric E. Fullerton, J. Magn. Magn. Mater. **320**, 1217 (2008)
[22] T. Devolder, Appl. Phys. Express **4**, 093001 (2011)
[23] J. Z. Sun, T. S. Kuan, J. A. Katine, Roger H. Koch, Proc. SPIE **5359**, 445 (2004)
[24] Ya. B. Bazaliy, B. A. Jones, and S. C. Zhang, J. Appl. Phys. **89**, 6793 (2001)
[25] Ya. B. Bazaliy and B. A. Jones, Physica B **329-333**, 1290 (2003).
[26] Ya. B. Bazaliy, B. A. Jones, and S. C. Zhang, Phys. Rev. B **69**, 094421 (2004)
[27] S. Urazhdin, H. Kurt, W. P. Pratt, and J. Bass, Appl. Phys. Lett. **83**, 114 (2003)
[28] S. Urazhdin, N. O. Birge, W. P. Pratt Jr., J. Bass, Phys. Rev. Lett. **91**, 146803 (2003)
[29] S. Urazhdin, Phys. Rev. B **69**, 134430 (2004)
[30] S. Urazhdin, H. Kurt, M. AlHajDarwish, Norman O. Birge, W. P. Pratt, J. Bass, J. Appl. Phys. **97**, 10C701 (2005)
[31] D. Lacour, J. A. Katine, N. Smith, M. J. Carey, J. R. Childress, Appl. Phys. Lett. **85**, 4681 (2004)
[32] S. I. Kiselev, J. C. Sankey, I. N. Krivorotov, N. C. Emley, M. Rinkoski, C. Perez, R. A. Buhrman, and D. C. Ralph, Phys. Rev. Lett. **93**, 036601 (2004)

[33] M. A. Zimmler, B. Özyilmaz, W. Chen, A. D. Kent, J. Z. Sun, M. J. Rooks, and R. H. Koch, Phys. Rev. B **70**, 184438 (2004)
[34] T. Devolder, A. Tulapurkar, Y. Suzuki, C. Chappert, P. Crozat, K. Yagami, J. Appl. Phys. **98**, 053904 (2005)
[35] J. C. Sankey, I. N. Krivorotov, S. I. Kiselev, P. M. Braganca, N. C. Emley, R. A. Buhrman, and D. C. Ralph, Phys. Rev. B **72**, 224427 (2005)
[36] B. Özyilmaz, A. D. Kent, M. J. Rooks, and J. Z. Sun, Phys. Rev. B **71**, 140403 (2005)
[37] M. L. Schneider, M. R. Pufall, W. H. Rippard, S. E. Russek, J. A. Katine, Appl. Phys. Lett. **90**, 092504 (2007)
[38] B. Özyilmaz and A. D. Kent, Appl. Phys. Lett. **88**, 162506 (2006)
[39] A. Deac, K. J. Lee, Y. Liu, O. Redon, M. Li, P. Wang, J. P. Nozières, B. Dieny, Phys. Rev. B **73**, 064414 (2006)
[40] A. Deac, Y. Liu, O. Redon, S. Petit, M. Li, P. Wang, J. P. Nozières, B. Dieny, J. Phys. Cond. Matter **19**, 165208 (2007)
[41] O. Ozatay, P. G. Gowtham, K. W. Tan, J. C. Read, K. A. Mkhoyan, M. G. Thomas, G. D. Fuchs, P. M. Braganca, E. M. Ryan, K. V. Thadani, J. Silcox, D. C. Ralph, R. A. Buhrman, Nature Mat. **7**, 567 (2008)
[42] N. Müsgens, E. Maynicke, M. Weidenbach, C. J. P. Smits, M. Bückins, J. Mayer, B. Beschoten and G. Güntherodt, J. Phys. D: Appl. Phys. **41**, 164011 (2008)
[43] I. Sodemann and Ya. B. Bazaliy, Phys. Rev. B **84**, 064422 (2011)
[44] J. Grollier, V. Cros, A. Hamzic, J. M. Georges, G. Faini, J. Ben Youssef, H. Le Gall, and A. Fert, Phys. Rev. B **67**, 174402 (2003)
[45] V. Cros, O. Boulle, J. Grollier, A. Hamzic, M. Munoz, L. G. Pereira, F. Petroff, C. R. Physique **6**, 956-965 (2005)
[46] H. Morise and S. Nakamura, Phys. Rev. B **71**, 014439 (2005)
[47] J. Xiao, A. Zangwill, and M. D. Stiles, Phys. Rev. B **72**, 014446 (2005)
[48] J. Z. Sun, D. J. Monsma, T. S. Kuan, M. J. Rooks, D. W. Abraham, B. Özyilmaz, A. D. Kent, and R. H. Koch, J. Appl. Phys. **93**, 6859 (2003)
[49] I. N. Krivorotov, N. C. Emley, A. G. F. Garcia, J. C. Sankey, S. I. Kiselev, D. C. Ralph, and R. A. Buhrman, Phys. Rev. Lett. **93**, 166603 (2004)
[50] S. Mangin, D. Ravelosona, J. A. Katine, M. J. Carey, B. D. Terris, and E. E. Fullerton, Nat. Mater. **5**, 210 (2006)
[51] S. Mangin, Y. Henry, D. Ravelosona, J. A. Katine, and Eric E. Fullerton, Appl. Phys. Lett. **94**, 012502 (2009)
[52] Ioan Tudosa, J. A. Katine, S. Mangin, and Eric E. Fullerton, Appl. Phys. Lett, **96**, 212504 (2010)
[53] W. Lin, J. Cucchiara, C. Berthelot, T. Hauet, Y. Henry, J. A. Katine, Eric E. Fullerton and S. Mangin, Appl. Phys. Lett **96**, 252503 (2010)
[54] D. Bedau, H. Liu, J-J. Bouzaglou, A. D. Kent J. Z. Sun, J. A. Katine, Eric E. Fullerton and S. Mangin, Appl. Phys. Lett **96**, 022514 (2010)
[55] N. Reckers, J. Cucchiara, O. Posth, C. Hassel, F. M. Römer, R. Narkowicz, R. A. Gallardo, P. Landenos, H. Zähres, S. Mangin, J. A. Katine, Eric E. Fullerton, G. Dumpich, R. Meckenstocvk, J. Lindner and M. Farle, Phys. Rev. B **83**, 184427 (2011)
[56] R. Zhu and P. B. Visscher, J. Appl. Phys. **103**, 07A722 (2008)
[57] T. Seki, S. Mitani, and K. Takanashi, Phys. Rev. B **77**, 214414 (2008)
[58] U. Ebels, D. Houssameddine, I. Firastrau, D. Gusakova, C. Thirion, B. Dieny, and L. D. Buda-Prejbeanu, Phys. Rev. B **78**, 024436 (2008)
[59] I. Firastrau, U. Ebels, L. D. Buda-Prejbeanu, J. C. Toussaint, C. Thirion, and B. Dieny, J. Magn. Magn. Mater. **310**, 2029 (2007)

[60] I. Firastrau, D. Gusakova, D. Houssameddine, U. Ebels, M-C. Cyrille, B. Delaet, B. Dieny, O. Redon, J. -C. Toussaint, L. D. Buda-Prejbeanu, Phys. Rev. B **78**, 024437 (2008)
[61] R-X. Wang, P-B. He, Z-D. Li, A-L. Pan, Q-H Liu, J. Appl. Phys. **109**, 033905 (2011)
[62] G. D. Fuchs, I. N. Krivorotov, P. M. Braganca, N. C. Emley, A. G. F. Garcia, D. C. Ralph, and R. A. Buhrman, Appl. Phys. Lett. **86**, 152509 (2005)
[63]Y. Higo, K. Yamane, K. Ohba, H. Narisawa, K. Bessho, M. Hosomi, H. Kano, Appl. Phys. Lett. **87**, 082502 (2005)
[64] M. Yoshikawa, T. Ueda, H. Aikawa, N. Shimomura, E. Kitagawa, M. Nakayama, T. Kai, K. Nishiyama, T. Nagase, T. Kishi, S. Ikegawa, H. Yoda, J. Appl. Phys. **101**, 09A511 (2007)
[65] J. Z. Sun, M. C. Gaidis, G. Hu, E. J. O'Sullivan, S. L. Brown, J. J. Nowak, P. L. Trouilloud, and D. C. Worledge, J. Appl. Phys. **105**, 07D109 (2009)
[66] J. Z. Sun, M. C. Gaidis, E. J. O'Sullivan, E. A. Joseph, G. Hu, D. W. Abraham, J. J. Nowak, P. L. Trouilloud, Yu Lu, S. L. Brown, D. C. Worledge, and W. J. Gallagher, Appl. Phys. Lett. **95**, 083506 (2009)
[67] J. Z. Sun, R. P. Robertazzi, J. Nowak, P. L. Trouilloud, G. Hu, D. W. Abraham, M. C. Gaidis, S. L. Brown, E. J. O'Sullivan, W. J. Gallagher, and D. C. Worledge, Phys. Rev. B **84**, 064413 (2011).
[68] J. Z. Sun, P. L. Trouilloud, M. J. Gajek, J. Nowak, R. P. Robertazzi, G. Hu, D. W. Abraham, M. C. Gaidis, S. L. Brown, E. J. O'Sullivan, J. Appl. Phys. **111**, 07C711 (2012)
[69] S-C. Oh, S-Y. Park, A. Manchon, M. Chshiev, J-H. Han, H-W. Lee, J-E. Lee, K-T. Nam, Y. Jo, Y-C. Kong, B. Dieny, K-J. Lee, Nature Phys. **5**, 898 (2009)
[70] S. Isogami, M Tsunoda, Y. Komasaki, A. Sakamura, M. Takahasi, Appl. Phys. Express **3**, 103002 (2010)
[71] T. Aoki, Y. Ando, M. Oogane, H. Naganuma, Appl. Phys. Express **3**, 053002 (2010)
[72] S-Y. Park, J-H. Han, S-C. Oh, J-E. Lee, K-T. Nam, H-W. Lee, Y. Jo, K-J. Lee, J. Phys. D Appl. Phys. **44**, 064008 (2011)
[73] D. C. Worledge, G. Hu, David W. Abraham, J. Z. Sun, P. L. Trouilloud, J. Nowak, S. Brown, M. C. Gaidis, E. J. O'Sullivan, and R. P. Robertazzi, Appl. Phys. Lett. **98**, 022501 (2011)
[74] K. Yagami, A. A. Tulapurkar, A. Fukushima, Y. Suzuki, J. Appl. Phys. **97**, 10C707 (2005)
[75] Y. Higo, K. Yamane, K. Ohba, H. Narisawa, K. Bessho, M. Hosomi, H. Kano, Appl. Phys. Lett. **87**, 082502 (2005)
[76] Z. Li, S. Zhang, Z. Diao, Y. Ding, X. Tang, D. M. Apalkov, Z. Yang, K. Kawabata, and Y. Huai, Phys. Rev. Lett. **100**, 246602 (2008)
[77] S. Yakata, H. Kubota, T. Sugano, T. Seki, K. Yakushiji, A. Fukushima, S. Yuasa, Koji Ando, App. Phys. Lett. **95**, 242504 (2009)
[78] K. Miura, R. Sugano, M. Ichimura, J. Hayakawa, S. Ikeda, H. Ohno, and S. Maekawa Phys. Rev. B **84**, 174434 (2011)
[79] T. Seki, S. Mitani, K. Yakushiji, and K. Takanashi, Appl. Phys. Lett. **88**,172504 (2006)
[80] H. Meng and J.-P. Wang, Appl. Phys. Lett. **88**, 172506 (2006)
[81] A. Kent, B. Ozyilmaz, and E. del Barco, Appl. Phys. Lett. **84**, 3897 (2004)
[82] K. J. Lee, O. Redon, and B. Dieny, Appl. Phys. Lett. **86**, 022505 (2005)
[83] H. Yoda, T. Kishi, T. Nagase, M. Yoshikawa, K. Nishiyama, E. Kitagawa, T. Daibou, M. Amano, N. Shimomura, S. Takahashi, T. Kai, M. Nakayama, H. Aikawa, S. Ikegawa, M. Nagamine, J. Ozeki, S. Mizukami, M. Oogane, Y. Ando, S. Yuasa, K. Yakushiji, H. Kubota, Y. Suzuki, Y. Nakatani, T. Miyazaki, K. Ando, Curr. Appl. Phys **10**, e87 (2010)
[84] I. Yulaev, M. Lubarda, S. Mangin, V. Lomakin, and Eric E. Fullerton, Appl. Phys. Lett **99**, 132502 (2011)
[85] Eric. E. Fullerton, S. Mangin, Nature Mat. **7**, 257 (2008)

[86] Y. Henry, S. Mangin, J. Cucchiara, J. A. Katine and Eric E Fullerton, Phys. Rev. B **79**, 214422 (2009)
[87] J. Z. Sun, D. J. Monsma, D. W. Abraham, M. J. Rooks, and R. H. Koch, Appl. Phys. Lett. **81**, 2202 (2002)
[88] R-X. Wang, P-B. He, Z-D. Li, A-L. Pan, Q-H. Liu, J. Appl. Phys. **109**, 033905 (2011)
[89] J. Kurkijärvi, Phys. Rev. B **6**, 832 (1972)
[90] D. B. Gopman, D. Bedau, S. Mangin, C-H. Lambert, Eric E. Fullerton, J. A. Katine, and A. D. Kent, Appl. Phys. Lett **100**, 062404 (2012)
[91] D. Bedau, H. Liu, J. Z. Sun, J. A. Katine, E. E. Fullerton, S. Mangin, and A. D. Kent, Appl. Phys. Lett. **97**, 262502 (2010)
[92] D. P. Bernstein, B. Bräuer, R. Kukreja, J. Stöhr, T. Hauet, J. Cucchiara, S. Mangin, J.A. Katine, T. Tyliszczak K. W. Chou and Y. Acremann, Phys. Rev. B **83**, 180410(R) (2011)
[93] J. Cucchiara, Y. Henry, D. Ravelosona, D. Lacour, Eric. E. Fullerton, J. A. Katine and S. Mangin, Appl Phys. Lett. **94**, 102503 (2009)
[94] J. R. Cash and Alan H. Karp, ACM Trans. on Math. Softw. **16**, 201 (1990)
[95] S. Girod, M. Gottwald, S. Andrieu, S. Mangin, J. McCord, Eric E. Fullerton, J.-M. L. Beaujour, B. J. Krishnatreya, and A. D. Kent, App. Phys. Lett. **94**, 262504 (2009)
[96] S. Chikazumi, *Physics of Ferromagnetism*, p. 249 (2nd edition, Oxford science publications, 1999)
[97] H. Neal Bertram and Vladimir L. Safonov, Appl. Phys. Lett. **79**, 4402 (2001)
[98] A. Shukh and J. van Ek, J. Appl. Phys. **91**, 8375 (2002)
[99] O. Posth, C. Hassel, M. Spasova, G. Dumpich, J. Lindner, and S. Mangin, J. Appl. Phys. **106**, 023919 (2009)
[100] M. Gottwald, S. Andrieu, F. Gimbert, E. Shipton, L. Calmels, C. Magen, E. Snoeck, M. Liberati , T. Hauet , E. Arenholz , S. Mangin , E. Fullerton, submitted to Phys. Rev. B (2012)
[101] S. Ikeda, K. Miura, H. Yamamoto, K. Mizunuma, H. D. Gan, M. Endo, S. Kanai, J. Hayakawa, F. Matsukura and H. Ohno, Nature Mat. **9,** 721 (2010)